Virtual Room Acoustics using Finite Difference Methods. How to Model and Analyse Frequency-Dependent Boundaries?

Konrad Kowalczyk and Maarten van Walstijn

Sonic Arts Research Centre (SARC)
School of Electronics, Electrical Engineering and Computer Science
Queen's University, Belfast, Northern Ireland
{kkowalczyk01, m.vanwalstijn}@qub.ac.uk

Abstract—In this paper, we present new methods for constructing and analysing frequency-dependent boundaries in room acoustic modelling with the use of finite difference time domain (FDTD) techniques. Novel FDTD formulations of simple locally reacting wall models with complex impedance are proposed and analysed in terms of pressure wave reflectance for different wall impedances and angles of incidence. The analysis is done using both numerical experiments and analytic evaluation.

For the numerical experiments, a compact implicit scheme of 4th-order accuracy is used for updating the room interior grid points, the results of which are analysed in both time and frequency domains. The simulation results show that the 2D frequency-dependent locally reacting wall models adhere well to their theoretical counterparts, particularly at low frequencies. Furthermore, they validate the analytic evaluation method, which paves the way for using either method as a tool for analysis of numerical reflectance.

Index Terms—Acoustic reflection, acoustic impedance, acoustic signal processing, FDTD methods, waveguides

I. INTRODUCTION

Finite Difference (FD) is a modelling technique that can be applied to room acoustic simulations [1]. Recent research efforts have focused on developing accurate FD approximations of realistic boundaries. Most of the boundary models available in the literature are based on a 1D approach [2], [3]. However, this leads to significant errors in the reflectance phase and amplitude [4]. For a physically more correct impedance boundary formulation, the boundary should be included in the medium, which can be obtained by combining the 1D boundary condition with the multi-dimensional (i.e. 2D or 3D) wave equation. Since frequency-dependent absorption occurs at realistic boundaries, the amplitude and phase of the reflected sound wave differ from those of the incident wave [5]. Instead of combining the FD implementation for the room interior with reflectance filters at boundaries [6], direct incorporation of the wall impedance in the boundary condition can be used. Alternative models rely on modelling the wave propagation in the wall [7]. However, previous studies [1] have suggested that there is no significant difference between the locally and

non-locally reacting wall models used in FD room acoustic simulations.

Sec. II presents the numerical formulation of the 2D FD frequency-dependent locally reacting wall models. In sec. III, an analytic evaluation method for the analysis of the numerical reflectance in 2D/3D acoustic spaces is presented. The results of numerical experiments and the numerical boundary analysis are discussed in sec. IV and V, respectively. Considerations here are restricted to 2D modelling; analogous 3D models will be dealt with in a subsequent paper.

II. FREQUENCY-DEPENDENT BOUNDARIES IN FD METHOD

Sound wave reflection from a wall can be modelled as a locally reacting wall (LRW), where the normal component of the particle velocity at the surface of the wall depends on the sound pressure in front of the wall element and not on pressure in front of neighbouring elements [5]. As such, it provides a compact model for simulating specular wall reflections. In terms of pressure only this may be stated as [4]

$$\frac{\partial p}{\partial t} = -c \frac{Z}{\rho c} \frac{\partial p}{\partial x}, \tag{1}$$

where p denotes acoustic pressure, c is the sound velocity and $Z/\rho c$ is the normalised wall impedance, also known as the specific acoustic impedance. The multi-dimensional FD formulation of a locally reacting wall is obtained by combining the discretised boundary condition (1) with the discrete multi-dimensional wave equation [4]. The reflectance R is related to the specific acoustic impedance by [5]

$$R = \frac{\frac{Z}{\rho c} \cos \theta - 1}{\frac{Z}{\rho c} \cos \theta + 1}, \tag{2}$$

where θ denotes the angle of incidence.

Real acoustic boundaries are generally frequency-dependent, even in narrow frequency bands. Among the simplest of such boundaries, we can distinguish two types. The first type represents heavy porous layers such as curtains or light non-stiff walls. The second one represents a thin absorbing layer stretched on the much harder boundary; seat,

floor and wall coverings are good examples. More complex boundaries can be formulated as a superposition of these two types [1].

A. Spring boundary

The first absorbing boundary type, representing materials such as a thin porous layer of fabric hung on a rigid wall [5], has the following impedance $Z = R + K/s$, where R denotes resistance, K is the spring constant, and s is the Laplace variable. Inserting such an impedance into Eq. (1) yields the continuous spring boundary condition

$$\frac{\partial p}{\partial t} = -c \left(\frac{R}{\rho c} \frac{\partial p}{\partial x} + \frac{K}{\rho c} \int_{-\infty}^{t} \frac{\partial p}{\partial x} dt \right). \tag{3}$$

The FD discrete boundary is obtained by approximating the first-order derivatives in time and space domains with centered FD operators. As for a numerical integration method, we propose the use of a composite trapezoidal rule with subintervals equal to time steps because of the method's accuracy and good phase properties. Conversely, the use of the backward Euler integration, which was applied in [1], would result in a less correct reflectance phase and amplitude. Trapezoidal integration is mathematically equivalent to the bilinear transform $s = \frac{2}{T} \frac{1-z^{-1}}{1+z^{-1}}$ applied to $y = x/s$, which yields

$$y^n = T \frac{x^n + x^{n-1}}{2} + y^{n-1}, \tag{4}$$

Consequently, numerical integration is given by

$$\frac{K}{\rho c} \int_{-\infty}^{t} p_{l,m}^n dt = \frac{TK}{2\rho c} \sum_{i=-\infty}^{n} \left(p_{l,m}^i + p_{l,m}^{i-1} \right). \tag{5}$$

If we write out the discrete version of the spring boundary condition for the point lying outside of the modelled space, also referred to as a 'ghost point', the following formula results

$$p_{l+1,m}^n = p_{l-1,m}^n + \frac{1}{\lambda(a_R + a_K)} (p_{l,m}^{n-1} - p_{l,m}^{n+1})$$
$$+ \frac{a_K}{a_R + a_K} (p_{l-1,m}^{n-1} - p_{l+1,m}^{n-1} + S_K^{n-1}), \tag{6}$$

where $\lambda = cT/X$ is the Courant number, X denotes grid spacing, T is a time step, $p_{l,m}^n$ is the pressure update variable, l and m denote spatial indexes and n is a time index, respectively. The parameters a_R and a_K are given in Table I and the new variable S_K is introduced for storage of the result of summation 'up to now' according to the formula

$$S_K^{n-1} = p_{l-1,m}^{n-1} - p_{l+1,m}^{n-1} + p_{l-1,m}^{n-2} - p_{l+1,m}^{n-2} + S_K^{n-2}. \tag{7}$$

Next, the update formula for the boundary node is obtained by substituting for the ghost point in a discrete 2D wave equation

$$p_{l,m}^{n+1} = \lambda^2 (p_{l+1,m}^n + p_{l-1,m}^n + p_{l,m+1}^n + p_{l,m-1}^n)$$
$$+ 2(1 - 2\lambda^2) p_{l,m}^n - p_{l,m}^{n-1}, \tag{8}$$

with the boundary condition given by Eq. (6), which yields

$$p_{l,m}^{n+1} = \left[\lambda^2 (2p_{l-1,m}^n + p_{l,m+1}^n + p_{l,m-1}^n) + 2(1 - 2\lambda^2) p_{l,m}^n \right.$$
$$+ (\frac{\lambda}{a_R + a_K} - 1) p_{l,m}^{n-1} + \frac{\lambda^2 a_K}{a_R + a_K} (p_{l-1,m}^{n-1} - p_{l+1,m}^{n-1})$$
$$+ \left. \frac{\lambda^2 a_K}{a_R + a_K} S_K^{n-1} \right] / \left(1 + \frac{\lambda}{a_R + a_K} \right). \tag{9}$$

This boundary formulation requires the update of the boundary node, the ghost point and the sum up to now at each time step according to Eq. (9), Eq. (6), and Eq. (7), respectively. However, only one previous value needs to be stored for both the ghost point and the sum value.

B. Mass boundary

The second boundary type, representing a nonporous layer hung in front of the rigid wall [5], defines an impedance as $Z = R + Ms$, where M denotes the mass per unit area. The continuous mass boundary condition is given by

$$\frac{\partial p}{\partial t} = -c \left(\frac{R}{\rho c} \frac{\partial p}{\partial x} + \frac{M}{\rho c} \frac{\partial p^2}{\partial t \partial x} \right) \tag{10}$$

All first-order derivatives in Eq. (10) are approximated with centered FD operators. Similarly to the spring boundary model, we propose the use of bilinear transform in the mixed second-order derivative. Alternative approach relying on the use of asymmetric backward Euler approximation, which was applied in [1], would bring about higher error in numerical reflectance. The discrete version of Eq. (10) for a ghost point then becomes

$$p_{l+1,m}^n = p_{l-1,m}^n + \frac{1}{\lambda(a_R + a_M)} (p_{l,m}^{n-1} - p_{l,m}^{n+1})$$
$$+ \frac{a_M}{a_R + a_M} (p_{l+1,m}^{n-1} - p_{l-1,m}^{n-1} + S_M^{n-1}), \tag{11}$$

where parameters a_R and a_M are given in Table I. The new variable S_M is introduced for storage of the result of the formula

$$S_M^{n-1} = p_{l+1,m}^{n-1} - p_{l-1,m}^{n-1} + p_{l-1,m}^{n-2} - p_{l+1,m}^{n-2} - S_M^{n-2}. \tag{12}$$

Substituting for the ghost point in the respective discrete wave equation (8) with the boundary condition (11), the update formula for the mass boundary node yields

$$p_{l,m}^{n+1} = \left[\lambda^2 (2p_{l-1,m}^n + p_{l,m+1}^n + p_{l,m-1}^n) + 2(1 - 2\lambda^2) p_{l,m}^n \right.$$
$$+ (\frac{\lambda}{a_R + a_M} - 1) p_{l,m}^{n-1} + \frac{\lambda^2 a_M}{a_R + a_M} (p_{l+1,m}^{n-1} - p_{l-1,m}^{n-1})$$
$$+ \left. \frac{\lambda^2 a_M}{a_R + a_M} S_M^{n-1} \right] / \left(1 + \frac{\lambda}{a_R + a_M} \right). \tag{13}$$

This boundary formulation requires updating the boundary node, the ghost point and summation S_M at each time step according to Eq. (13), Eq. (11), and Eq. (12), respectively. Only one past value needs to be stored for both the ghost point and variable S_M.

TABLE I
COMPLEX IMPEDANCE PARAMETERS.

Parameter	Description
$a_R = \frac{R}{\rho c}$	Specific resistance
$a_K = \frac{TK}{2\rho c}$	Specific spring constant multiplied by half of T
$a_M = \frac{2M}{T\rho c}$	Two times specific mass divided by T
$a = a_R + a_K + a_M$	Sum of the previous parameters

C. Combined impedance boundary

Some realistic acoustic boundaries might require a more complex impedance; parquet is a good example. Another example is a porous layer of fabric stretched in front of the rigid wall, to which the second layer of nonporous material hung immediately in front of the first layer is added [5]. The resulting boundary condition for a combined impedance $Z = R + Ms + K/s$ amounts to

$$\frac{\partial p}{\partial t} = -c\left(\frac{R}{\rho c}\frac{\partial p}{\partial x} + \frac{M}{\rho c}\frac{\partial p^2}{\partial t \partial x} + \frac{K}{\rho c}\int_{-\infty}^{t}\frac{\partial p}{\partial x}dt\right), \quad (14)$$

The derivation relies on the combination of the previously presented boundary models. Hence, the node at the boundary is updated according to

$$p_{l,m}^{n+1} = \left[\lambda^2(2p_{l-1,m}^n + p_{l,m+1}^n + p_{l,m-1}^n) + 2(1-2\lambda^2)p_{l,m}^n\right.$$
$$+ (\frac{\lambda}{a}-1)p_{l,m}^{n-1} + \frac{\lambda^2(a_K - a_M)}{a}(p_{l-1,m}^{n-1} - p_{l+1,m}^{n-1})$$
$$+ \left.\frac{\lambda^2 a_K}{a}S_K^{n-1} + \frac{\lambda^2 a_M}{a}S_M^{n-1}\right] / \left(1 + \frac{\lambda}{a}\right), \quad (15)$$

and the update formula for the ghost point is given by

$$p_{l+1,m}^n = p_{l-1,m}^n + \frac{1}{\lambda a}(p_{l,m}^{n-1} - p_{l,m}^{n+1}) + \frac{a_K - a_M}{a}$$
$$\cdot (p_{l-1,m}^{n-1} - p_{l+1,m}^{n-1}) + \frac{a_K}{a}S_K^{n-1} + \frac{a_M}{a}S_M^{n-1}, (16)$$

where the parameters a_R, a_K, a_M, and a are given in Table I, and the variables S_K and S_M are given by Eq. (7) and Eq. (12), respectively. All in all, Eq. (15), Eq. (16), Eq. (7), and Eq. (12) need to be computed at each time step.

III. ANALYTIC EVALUATION METHOD

In this section, a novel method for analytic evaluation of the numerical reflection of multi-dimensional boundaries is presented. Due to the limited space, this paper outlines briefly the concept behind the numerical boundary analysis (NBA) and presents the final formula for the numerical reflectance of the combined impedance model.

Consider a wall normal to the rectangular coordinate system in the x-y plane, where the wall is located at $x = 0$. An incident wave propagating at any oblique angle of incidence θ in a positive x-direction in such a system can be expressed as [5]

$$p = P_0\, e^{j\omega t}\, e^{-jk(x\cos\theta + y\sin\theta)}, \quad (17)$$

where P_0 is the incident wave amplitude and k denotes the wave number. As for the reflected wave, the sign is reversed and the pressure amplitude is multiplied by the reflection factor. Hence the total sound pressure in the standing wave in the plane of the locally reacting wall can be obtained by adding both incident and reflected sound pressure values and setting $x = 0$, which in the discrete space-time domain takes the following form

$$p_{l,m}^n = P_0\, e^{j\omega nT}e^{-j\tilde{k}mX\sin\theta}\left(e^{-j\tilde{k}lX\cos\theta} + \widehat{R}\, e^{j\tilde{k}lX\cos\theta}\right). \quad (18)$$

Eq. (18) can be used as a basis for deriving other discrete pressure values in the respective boundary equation. Some example expressions are given below

$$p_{l,m}^{n+1} = e^{j\omega T}\, p_{l,m}^n = e^{sT}\, p_{l,m}^n = z\, p_{l,m}^n, \quad (19)$$
$$p_{l-1,m}^n = P_0\, e^{j\omega nT}\, e^{-j\tilde{k}mX\sin\theta}$$
$$\cdot \left(e^{-j\tilde{k}(l-1)X\cos\theta} + \widehat{R}\, e^{j\tilde{k}(l-1)X\cos\theta}\right). \quad (20)$$

Next, we substitute such discrete pressure values in the discrete boundary equation and set $l = 0$, which corresponds to $x = 0$ at a boundary. Finally, the analytic evaluation method relies on solving for the numerical reflectance $\widehat{R}$. In case of the combined impedance boundary condition given by Eq. (15) the following formula results

$$\widehat{R}(z,\theta) = -\left\{\left(1+\frac{\lambda}{a}\right)z - \left[2\lambda^2 A + \lambda^2(B + B^{-1})\right.\right.$$
$$+ 2(1-2\lambda^2)\left] + z^{-1}\left[(1-\frac{\lambda}{a}) + (A^{-1} - A)\right.\right.$$
$$\left.\left.\cdot \left(\frac{\lambda^2 a_K}{a}\frac{2}{1-z^{-1}} - \frac{\lambda^2 a_M}{a}\frac{2}{1+z^{-1}}\right)\right]\right\}$$
$$/ \left\{\left(1+\frac{\lambda}{a}\right)z - \left[2\lambda^2 A^{-1} + \lambda^2(B + B^{-1})\right.\right.$$
$$+ 2(1-2\lambda^2)\left] + z^{-1}\left[(1-\frac{\lambda}{a}) + (A - A^{-1})\right.\right.$$
$$\left.\left.\cdot \left(\frac{\lambda^2 a_K}{a}\frac{2}{1-z^{-1}} - \frac{\lambda^2 a_M}{a}\frac{2}{1+z^{-1}}\right)\right]\right\}, \quad (21)$$

where $A = e^{j\tilde{k}X\cos\theta}$ and $B = e^{j\tilde{k}X\sin\theta}$. The wavenumber $\tilde{k}$ has to be computed from the dispersion equation, which for the 2D rectilinear scheme is given by

$$2\sin^2\left(\frac{\omega T}{2}\right) = \left[\sin^2\left(\frac{X\tilde{k}\cos\theta}{2}\right) + \sin^2\left(\frac{X\tilde{k}\sin\theta}{2}\right)\right]. \quad (22)$$

Eq. (21) can be used to predict accurately the numerical reflectance for any value of the impedance and angle of incidence. This formula is valid for up to the effective cut-off in the θ-direction (e.g. there are no resonances above $0.25f_s$ in axial directions for wave propagation in the 2D rectilinear scheme). Furthermore, the NBA reflectance magnitude does not outstrip unity in the range up to the Nyquist frequency, which guarantees stability of the simulation. The amplitude of the analytically evaluated numerical reflectance (solid lines) in

the frequency domain for the boundary models derived in this paper is presented in figures 3, 4, and 5, respectively. Note that the evaluation method requires the same multi-dimensional FD scheme for the boundary and the medium inside of the modelled space. Consequently, this method is not suitable for the evaluation of the 1D boundaries in a 2D/3D context.

IV. NUMERICAL EXPERIMENTS

A. Test setup

A number of simulations were carried out to analyse the performance of the three types of frequency-dependent boundary conditions of a locally reacting wall derived in section II. A fourth-order accurate compact implicit scheme [8] with 1800x1400 junctions was used for the implementation of the interior of the room in order to obtain the wavefront that was as flat as possible. The size of the room and the simulation time (2000 samples at the sample rate of 4kHz) were set in such a way that only the reflections from the investigated boundary could reach a receiver position. Furthermore, the simulation time had to be sufficiently long so that the whole wavelet could reach a receiver position. Each test consisted of two simulations, in which a sharp impulse was injected into a mesh point. In each test, the source position was chosen so that (1) a constant distance of 400 grid points from the centre of the investigated wall was preserved, and (2) the incident waves at the following angles of incidence $\theta = 0^o, 15^o, 30^o, 45^o, 60^o, 75^o$, resulted. In the first simulation, the reflected signal x_f was measured at a receiver position located at the same distance from the centre of the wall as a source; x_f inevitably included the 'direct sound'. The wall was removed in the second simulation and two signals were measured: the direct sound x_d at the same receiver position and the freefield signal x_i at the mirror location of the receiver. The isolated reflected signal x_r was obtained by $x_r = x_f - x_d$.

For the time domain analysis, the ideal time domain signal was obtained as a time domain convolution of the freefield signal x_i and the signal obtained from the inverse Laplace transform of the theoretical reflectance given by Eq. (2). The choice of the Laplace transform was made to avoid the characteristic ripples due to the inverse Fourier transforms. In order to reduce truncation error, the resulting signal was convolved with a 41-tap low pass FIR filter with a normalised cut-off frequency of 0.25. For the frequency domain plots, the numerical reflectance was defined as the deconvolution of x_r and x_i and the theoretical reflectance given by Eq. (2) was used as a reference. Furthermore, all the measured signals were windowed with the use of the right half of the Hanning window to reduce signal truncation errors.

B. Time domain analysis

A reflected sound wave has both phase and amplitude which differ from those of an incident wave if the boundary has a complex impedance. In this section, the phase of numerical boundary models is analysed through the time domain comparison of the reflected signals obtained from numerical experiments with the ideal reflection signals. Two representative
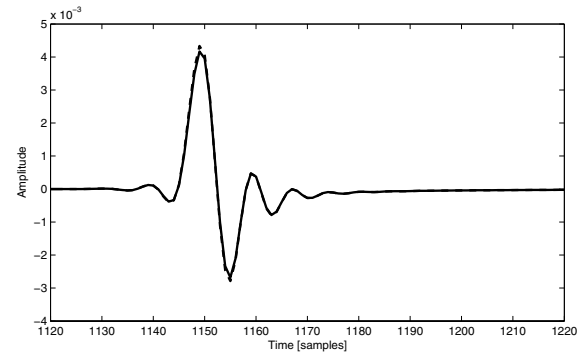

Fig. 1. Reflected signal (solid line) plotted against the theoretical reflection signal (dashed line) for the 2D spring boundary model at the angle of incidence $\theta = 60^o$, where $a_R = 9$ and $a_K = 0.5$.
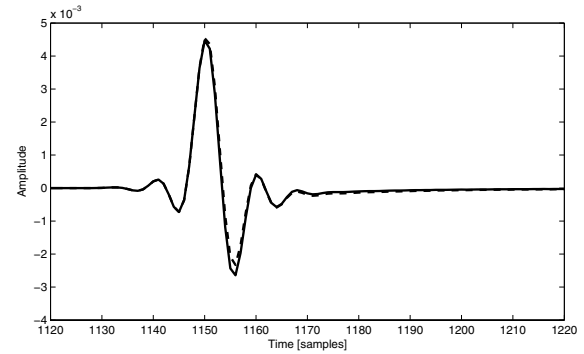

Fig. 2. Reflected signal (solid line) plotted against the theoretical reflection signal (dashed line) for the 2D combined impedance boundary model at the angle of incidence $\theta = 45^o$, where $a_R = 9$, $a_K = 0.5$, and $a_M = 10$.

results are illustrated in Fig. 1 and Fig. 2, namely the spring boundary with $a_R = 9$ and $a_K = 0.5$ for an incident angle $\theta = 60^o$ and the combined impedance boundary with $a_R = 9$, $a_K = 0.5$, $a_M = 10$ for incident angle $\theta = 45^o$; respectively. As depicted in Fig. 1, the spring boundary model preserves the phase perfectly and the amplitude is very well matched. Similarly, Fig. 2 confirms that in the case of the combined impedance boundary the phase is also well preserved. Such a correct phase characteristic is down to the use of bilinear transform which has excellent phase properties. Consequently, even at very high angles of incidence the reflectance phase is correct, which is not the case for 1D boundary models [4].

C. Reflectance magnitude analysis

In this section, the frequency-dependent reflectance amplitude is analysed in the frequency domain. The reflectance magnitudes of the three types of boundary conditions derived in section II are illustrated in figures 3, 4, and 5, for a variety of parameters and incident angles. All figures plot the reflectance obtained from numerical experiments (dashed lines), the reflectance predicted with the use of the analytic evaluation method (solid lines) and the theoretical reflection (dotted lines).

The theoretical reflection coefficient is matched well in general for up to a quarter of the sample rate for all the boundary
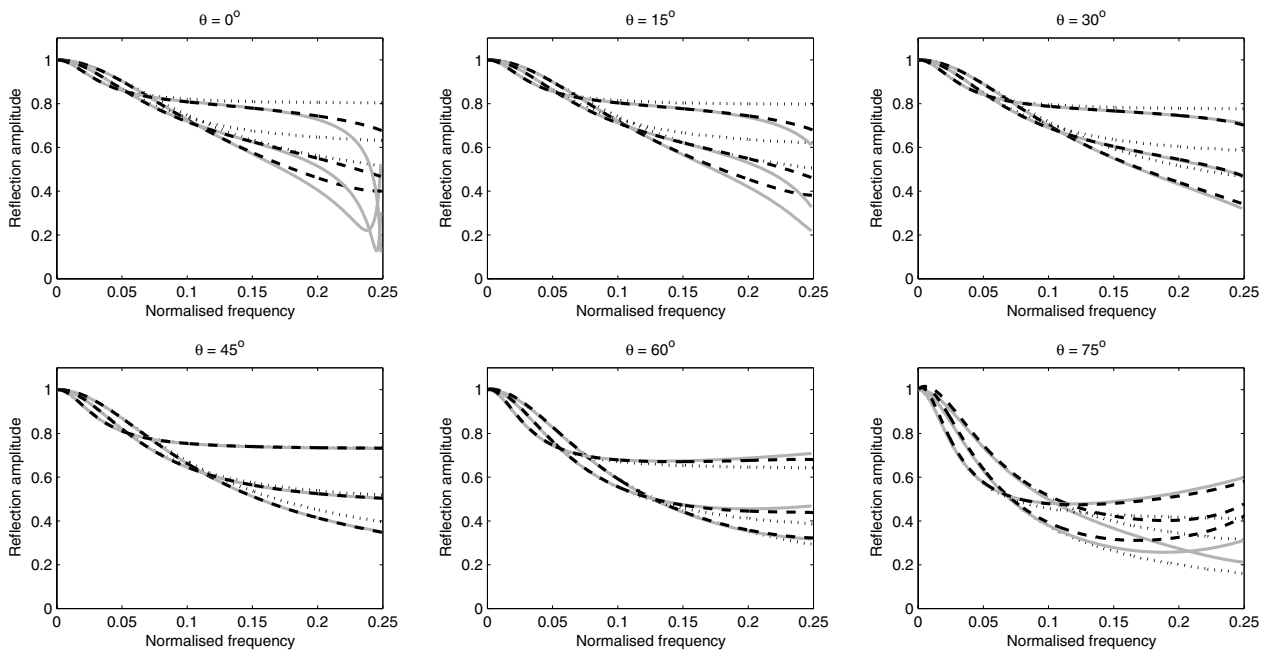
Fig. 3.   Numerical reflection of the spring boundary for the following values of parameters $a_R = \frac{7}{3}, 4, 9$, $a_K = 0.5$ and angles of incidence $\theta = 0^o, 15^o, 30^o, 45^o, 60^o, 75^o$. Dashed lines denote the reflectance obtained from numerical measurements, dotted lines denote the theoretical value of the reflection coefficient, and grey solid lines represent numerical reflectance obtained from the analytic evaluation method.
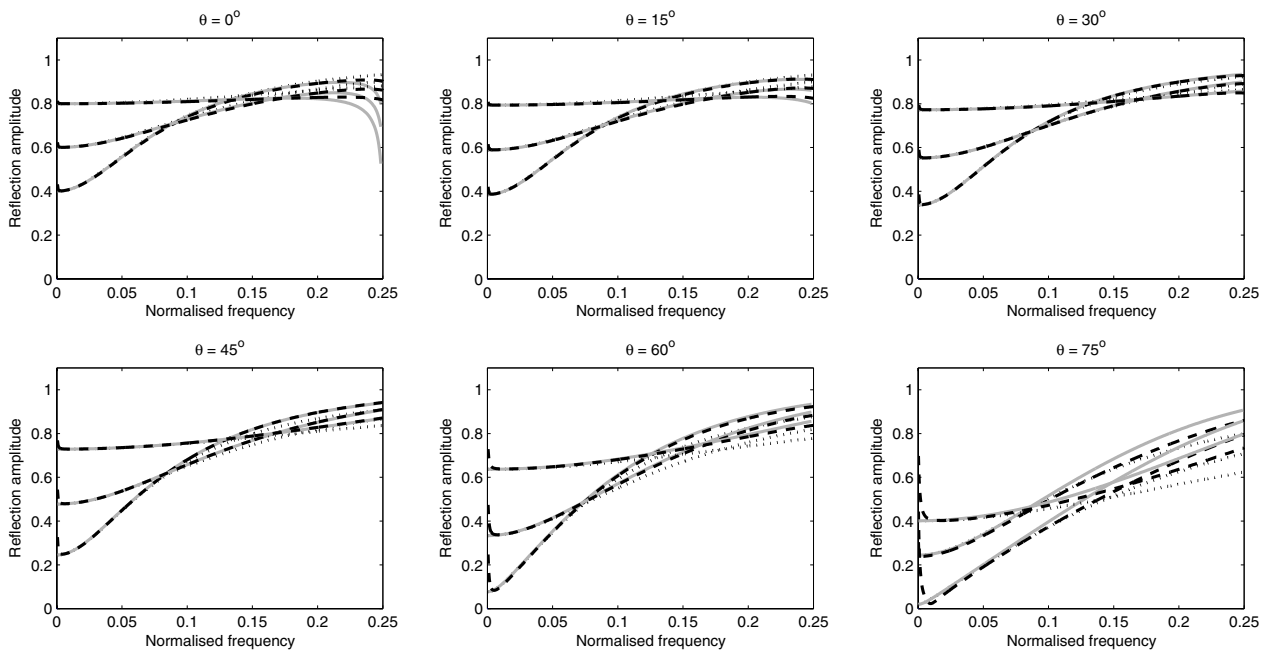

Fig. 4.   Numerical reflection of the mass boundary for the following values of parameters $a_R = \frac{7}{3}, 4, 9$, $a_M = 10$ and angles of incidence $\theta = 0^o, 15^o, 30^o, 45^o, 60^o, 75^o$. Dashed lines denote the reflectance obtained from numerical measurements, dotted lines denote the theoretical value of the reflection coefficient and grey solid lines represent numerical reflectance obtained from the analytic evaluation method.

models. The numerical reflectance differs the most at normal incidences, which coincides with the fact that the numerical dispersion of the 2D rectilinear scheme is the strongest in axial direction. Furthermore, the numerical reflectance adheres well at low frequencies for all models, which is a desirable feature of FD models of rooms. The discrepancy near DC ($\omega = 0$), particularly visible at very high angles of incidence, is due to truncation error and the waves being not perfectly plane at the point of reflection. It should be stressed that the theoretical reflection coefficient was derived for plane
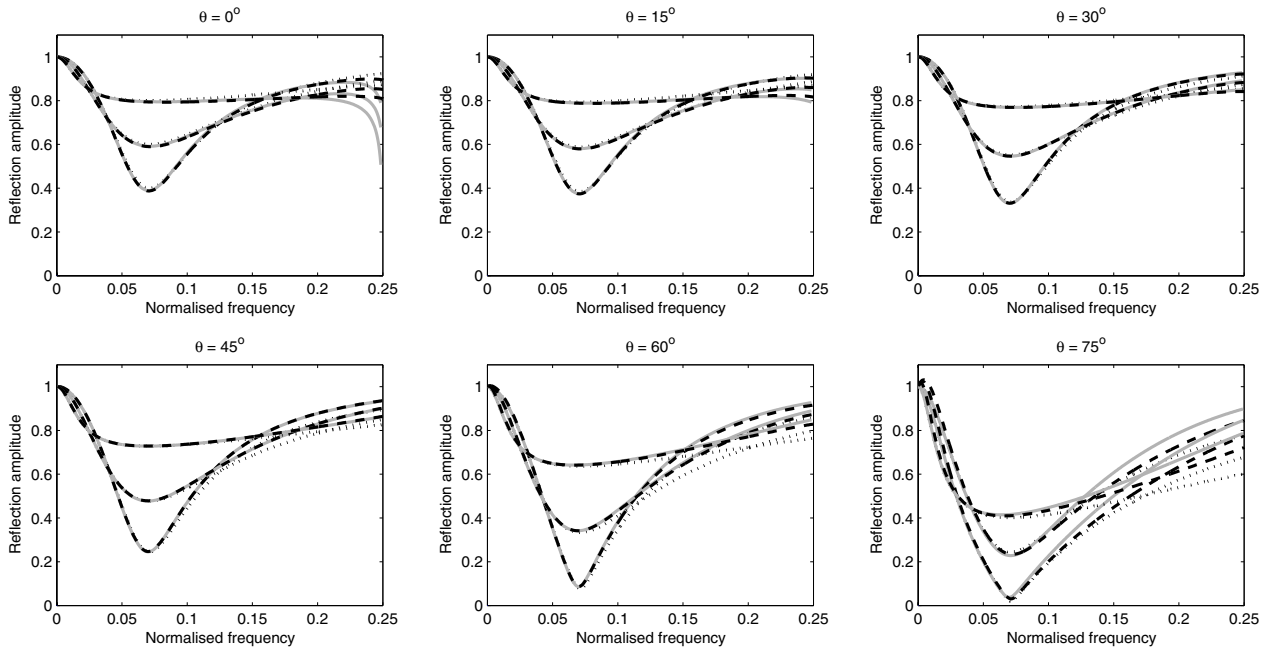
Fig. 5. Numerical reflection of a combined impedance boundary for the following values of parameters $a_R = \frac{7}{3}, 4, 9$, $a_K = 0.5$, $a_M = 10$ and angles of incidence $\theta = 0^o, 15^o, 30^o, 45^o, 60^o, 75^o$. Dashed lines denote the reflectance obtained from numerical measurements, dotted lines denote the theoretical value of the reflection coefficient, and grey solid lines represent numerical reflectance obtained from the analytic evaluation method.

waves, whereas in the experiments a spherical wave was used for the excitation. Even though the curvature of a spherical wavefront after traveling a long distance before hitting the wall can be neglected, a minor discrepancy remains. The analytic evaluation plots confirm that a sudden outstrip near DC does not really occur for these boundary models.

V. NUMERICAL BOUNDARY ANALYSIS RESULTS

The correctness of the NBA is confirmed by the perfect match of the measured and evaluated reflectance in figures 3, 4, and 5 for the angle of incidence $\theta = 45^o$ at which both the rectilinear scheme used in analytic evaluation formula derivation and the compact implicit scheme used for the room interior in numerical tests have no dispersion. There is also a good match for all possible angles of incidence and impedance values at low frequencies, where almost no numerical error occurs. In addition, the difference between the simulated and analytically evaluated numerical reflectance at high frequencies is due only to using a different scheme for the room interior. A closer match of the reflectance obtained from experiments than from NBA indicates that, despite the scheme discontinuity, a combination of the ADI method with these three boundary models leads to a more accurate numerical reflectance.

VI. CONCLUSION

The new multi-dimensional frequency-dependent locally reacting wall models preserve the phase well even at high angles of incidence. Furthermore, the reflectance magnitude adheres well at low frequencies for all presented models, which is not the case for the 1D termination of multi-dimensional

mesh simulations [4]. Consequently, such models provide a improved numerical formulation of frequency-dependent boundaries that can be applied in FD simulations of acoustic spaces.

In addition, an analytic evaluation method has been presented which can be used to predict the numerical reflectance for any impedance and angle of incidence in a fast and reliable way. As such, it provides a valuable tool for numerical reflectance analysis since the reflectance is deprived of artefacts which result from numerical experiments.

REFERENCES

[1] D. Botteldooren, "Finite-difference time-domain simulation of low-frequency room acoustic problems," *J. Acoustical Society America*, vol. 98, no. 6, pp. 3302–3308, 1995.
[2] L. Savioja, T. Rinne, and T. Takala, "Simulation of room acoustics with a 3-D finite difference mesh," *Proc. Int. Computer Music Conf. (ICMC)*, pp. 463–466, September 1994, Aarhus, Denmark.
[3] J. Huopaniemi, L. Savioja, and M. Karjalainen, "Modelling of reflections and air absorption in acoustical spaces - a digital filter design approach," *Proc. IEEE Workshop on Appl. of Signal Processing to Audio and Acoustics (WASPAA)*, October 1997.
[4] K. Kowalczyk and M. van Walstijn, "Formulation of a locally reacting wall in Finite Difference modelling of acoustic spaces," *Proc. Int. Symp. Room Acoustics (ISRA)*, pp. 1–6, September 2007, Seville, Spain.
[5] H. Kuttruff, *Room acoustics*, Applied Science Publishers Ltd, London, 1973.
[6] D.T. Murphy and M. Beeson, "The KW-boundary hybrid digital waveguide mesh for room acoustics applications," *IEEE Transactions on Speech and Audio Processing*, vol. 12, no. 2, pp. 552–564, 2007.
[7] A. Kelloniemi, "Improved adjustable boundary condition for the 2-D digital waveguide mesh," *Proc. Int. Conf. Digital Audio Effects (DAFx'05)*, September 2005.
[8] K. Kowalczyk and M. van Walstijn, "On-line simulation of 2D resonators with reduced dispersion error using compact implicit finite difference methods," *Proc. IEEE Int. Conf. Acoustics, Speech and Signal Processing (ICASSP)*, vol. 1, pp. 285–288, April 2007, Honolulu, Hawaii.